

## Dynamic behavior and microstructure characterization of TaNbHfZrTi high-entropy alloy at a wide range of strain rates and temperatures

Meng-lei Hu<sup>a</sup>, Wei-dong Song<sup>a,\*</sup>, Da-bo Duan<sup>b</sup>, Yuan Wu<sup>b</sup>

<sup>a</sup> State Key Laboratory of Explosion Science and Technology, Beijing Institute of Technology, Beijing 100081, China

<sup>b</sup> State Key Laboratory for Advanced Metals and Materials, University of Science and Technology Beijing, Beijing 100083, China



### ARTICLE INFO

#### Keywords:

High-entropy alloy  
Dynamic compression  
Crystallographic texture  
Strain rate  
Johnson-Cook model

### ABSTRACT

The TaNbHfZrTi refractory high-entropy alloy (RHEA) is suction casted by vacuum arc melting furnace. The mechanical behavior of the TaNbHfZrTi RHEA is systematically investigated through material testing machine and Split Hopkinson Pressure Bar (SHPB) system at strain rate up to  $2600\text{s}^{-1}$  and temperatures from 77K to 873K. Significant increases in the yield strength and interesting changes in strain rate sensitivity at high strain rates and high temperatures are observed. During the dynamic tests, the strain rate sensitivity rises from ~5 to ~76 with the temperature increases from 293K to 673K, demonstrating that high temperature has a significant influence on the strain rate effect of the TaNbHfZrTi RHEA. The comprehensive analysis of electron backscatter diffraction (EBSD) and Kernel Average Misorientation (KAM) technique shows that the pronounced homogeneous deformation microstructures exist in the sample even at the true strain of about 0.34, only very short adiabatic shear band (ASB) initiates. The fracture morphology investigated by scanning electron microscopy (SEM) indicates both ductile and brittle fracture behavior of the TaNbHfZrTi RHEA at 77K. The improved Johnson-Cook (J-C) model is proposed to describe the deformation behavior, in which both strain rate hardening and temperature softening terms are expressed as a function of strain and strain rate, respectively.

### 1. Introduction

High-entropy alloys (HEAs) as potential functional materials have attracted widespread concern due to their excellent physical and mechanical properties [1-10]. The multi-principal solid solution phase formed during the solidification of these HEAs is very stable, especially under high temperature conditions [11]. HEAs typically having five or more substantially equimolar concentrations of elements are necessary to achieve high mixing entropy. This concept possesses the advantage of producing solid solution alloys with simple face centered cubic (FCC) and/or body centered cubic (BCC) crystal structures [12-14]. The HEAs with single BCC structures consisting mainly of refractory metal elements are called refractory high entropy alloys (RHEAs) [1,15,16], which exhibit remarkable mechanical properties in extreme environments [17]. Because of their superior mechanical performance, RHEAs are now considered as potential candidates for replacement of Ni-based superalloys. While most of the mechanical experiments about RHEAs are performed in quasi-static state at room temperature [18-21], the high temperature mechanical tests need more attention [22,23]. In addition, many experiments have been performed to explore the effects of metal elements proportion or the element substitutions on the phase transformation and microstructure evolution of the RHEAs [19, 24, 25].

The most frequently used compositions of RHEAs are TaNbHfZrTi [11, 18, 22, 26-30], MoNbTaW and MoNbTaVW [31, 32]. The TaNbHfZrTi RHEA with a single BCC phase after gravity casting or suction-assisted casting process displays both high yield strength and good plasticity [1, 17].

Compression tests of TaNbHfZrTi after hot isostatically pressed and homogenized processes were carried out in the strain rate range of  $10^{-1}\text{s}^{-1} \sim 10^{-5}\text{s}^{-1}$  under high temperatures by Senkov et al. [22]. The experimental results showed that the material maintained a stable flow stress state while being uniformly deformed. Furthermore, the quasi-static tensile behaviors and microstructure of TaNbHfZrTi after rolling and annealing at different annealing temperatures were investigated [33]. Chen et al. [18] explored the influence of annealing time on the precipitation phases of different lattice structures by using a series of microscopic characterization techniques and further discovered preferred orientations of these precipitation phases with the BCC matrix in TaNbHfZrTi RHEA. What's more, the ultra-fine graining of TaNbHfZrTi by high pressure torsion straining could significantly increase the material strength while maintaining good plasticity [20]. In the study of the influence of cooling rate on the solidification structure of TaNbHfZrTi, Couzinié et al. [21] found that the region with a fast cooling rate was relatively uniform and the region with a slow cooling rate

\* Corresponding author.

E-mail address: [swdgh@bit.edu.cn](mailto:swdgh@bit.edu.cn) (W.-d. Song).

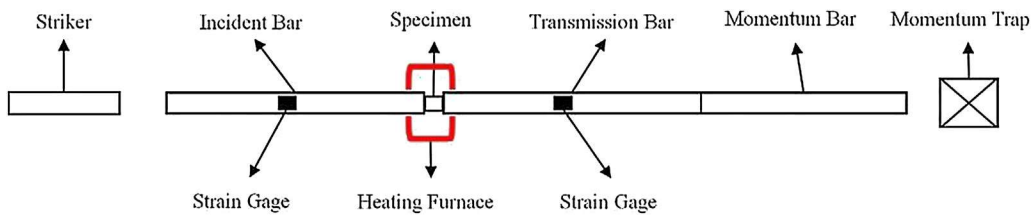


Fig. 1. The schematic of the SHPB test configuration equipped with a heating furnace.

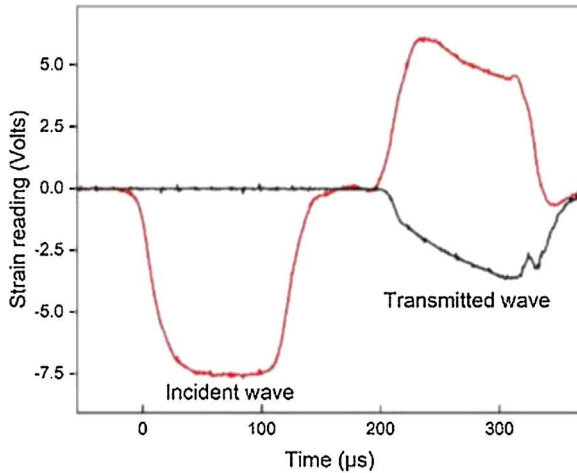


Fig. 2. Typical oscilloscope trace for TaNbHfZrTi RHEA sample at strain rate of  $1600\text{s}^{-1}$  and temperature of 293K.

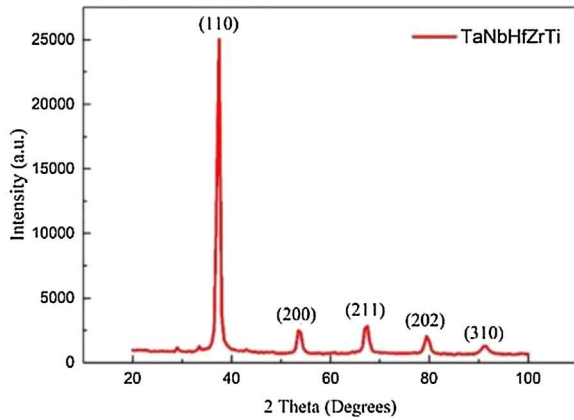


Fig. 3. XRD spectra of the suction-assisted cast TaNbHfZrTi RHEA sample before compression tests.

exhibited a micro-segregated dendritic structure with Ti, Zr and Hf enrichment.

As mentioned above, the mechanical property study on HEAs is mainly concentrated on the quasi-static regime. However, so far, the exploration of the dynamic mechanical response and microstructure deformation mechanism of HEAs is relatively limited. Dynamic shear tests on CrMnFeCoNi HEA were conducted by Li et al. [34] to explore the evolution of adiabatic shear band. They pointed out that the protraction of shear localization was related to the prominent work hardening effect and temperate thermal softening of CrMnFeCoNi HEA. Kumar et al. [35] revealed that Al<sub>0.1</sub>CoCrFeNi HEA with single phase FCC structure exhibited favorable ductility and low yield stress during high strain rate tests. Besides, Jiao et al. [36] noted that the AlCoCrFeNiTi<sub>x</sub> HEA with high yield strength and high fracture strain displayed positive strain rate

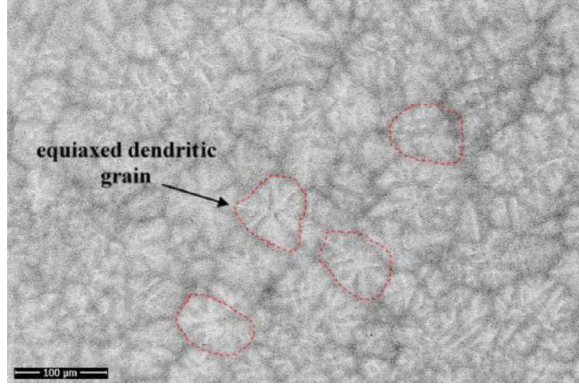
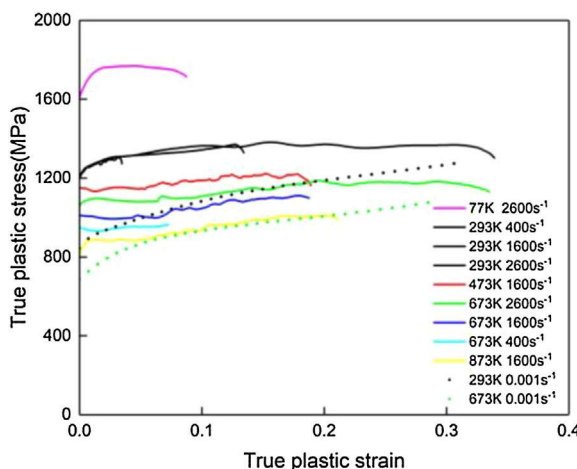


Fig. 4. SEM-BSE image on microstructure of the suction-assisted cast TaNbHfZrTi RHEA sample before tests.

sensitivity and strong strain hardening behavior under dynamic regime. For RHEAs, the strong shear localization of as-cast TaNbHfZrTi RHEA at high strain rate was observed by Dirras et al. [26] and they pointed out that the high strength under dynamic test was mainly attributed to high dislocation density.

As known, superalloys are usually applied to high temperature components of aircraft turbine jet engines, such as turbine blades, compressor as well as engine blade containment system [37]. The engine blade containment system usually consists of a metal alloy ring which is strong and ductile enough to prevent impact and penetration of a turbine blade in dangerous conditions. As far as known, aluminum alloys and some other relatively light metal materials are currently in application of blade containment systems [38]. Although light metal alloys can reduce the weight, the surrounding parts of the turbine region and combustor often encounter high/low temperature operation environment and high strain rate extreme conditions. Therefore, it is necessary to use high/low temperature metal alloys in jet engine components. According to the literatures, RHEAs are becoming potential materials in aerospace engineering for replacement of Ni-based superalloys due to their high yield strength and unique high temperature softening resistance. TaNbHfZrTi RHEA is the most frequently investigated material which exhibits a good trade-off between strength and ductility under quasi-static conditions. Therefore, in view of the application of aircraft turbine engine components especially the engine blade containment, it is of great significance to explore the dynamic mechanical property and microstructure evolution of TaNbHfZrTi RHEA at a series of strain rates and temperatures.

The present work focuses on the dynamic mechanical behaviors of the suction-assisted cast TaNbHfZrTi RHEA under temperatures of 77K ~ 873K. The effects of temperature and strain rate on the dynamic mechanical behavior of the suction-assisted cast TaNbHfZrTi RHEA are analyzed in detail. Post examinations under scanning electron microscopy (SEM) are performed on fractured TaNbHfZrTi sample after dynamic compression test at liquid nitrogen temperature to determine the fracture mechanism. The microstructure evolution under high strain rates loading at elevated temperatures are systematically characterized by op-



**Fig. 5.** True plastic stress-strain curves of the suction-assisted cast TaNbHfZrTi RHEA samples under different loading conditions (strain rates ranging from  $0.001\text{s}^{-1}$  to  $2600\text{s}^{-1}$  and temperatures ranging from 77K to 873K).

tical microscopy (OM), backscatter electron (BSE) imaging and electron backscatter diffraction (EBSD) to clarify the microscopic deformation mechanism. Furthermore, an improved Johnson-Cook (J-C) constitutive model is established to describe the high strain rate deformation behavior of TaNbHfZrTi RHEA.

## 2. Materials and experimental procedures

### 2.1. Sample preparation and microstructure investigation

The preparation method of obtaining the TaNbHfZrTi RHEA sample is as follows: the residual oxygen in the chamber is absorbed by melting the titanium getter before melting the refractory alloy, otherwise the prepared sample will be oxidized. High purity master alloys Ta-Zr and Nb-Hf-Ti with a purity exceeding 99.9% are arc-melted on a water-cooled copper plate under argon atmosphere. All the casting ingots are arc remelted at least eight times to eliminate chemical inhomogeneity, and eventually drop-cast into a  $15\text{mm}\times 15\text{mm}\times 30\text{mm}$  copper mold. The suction-assisted cast ingots are machined into cylindrical specimens with two kinds of size by electrical discharging machining and lathe for quasi-static compression tests and dynamic compression

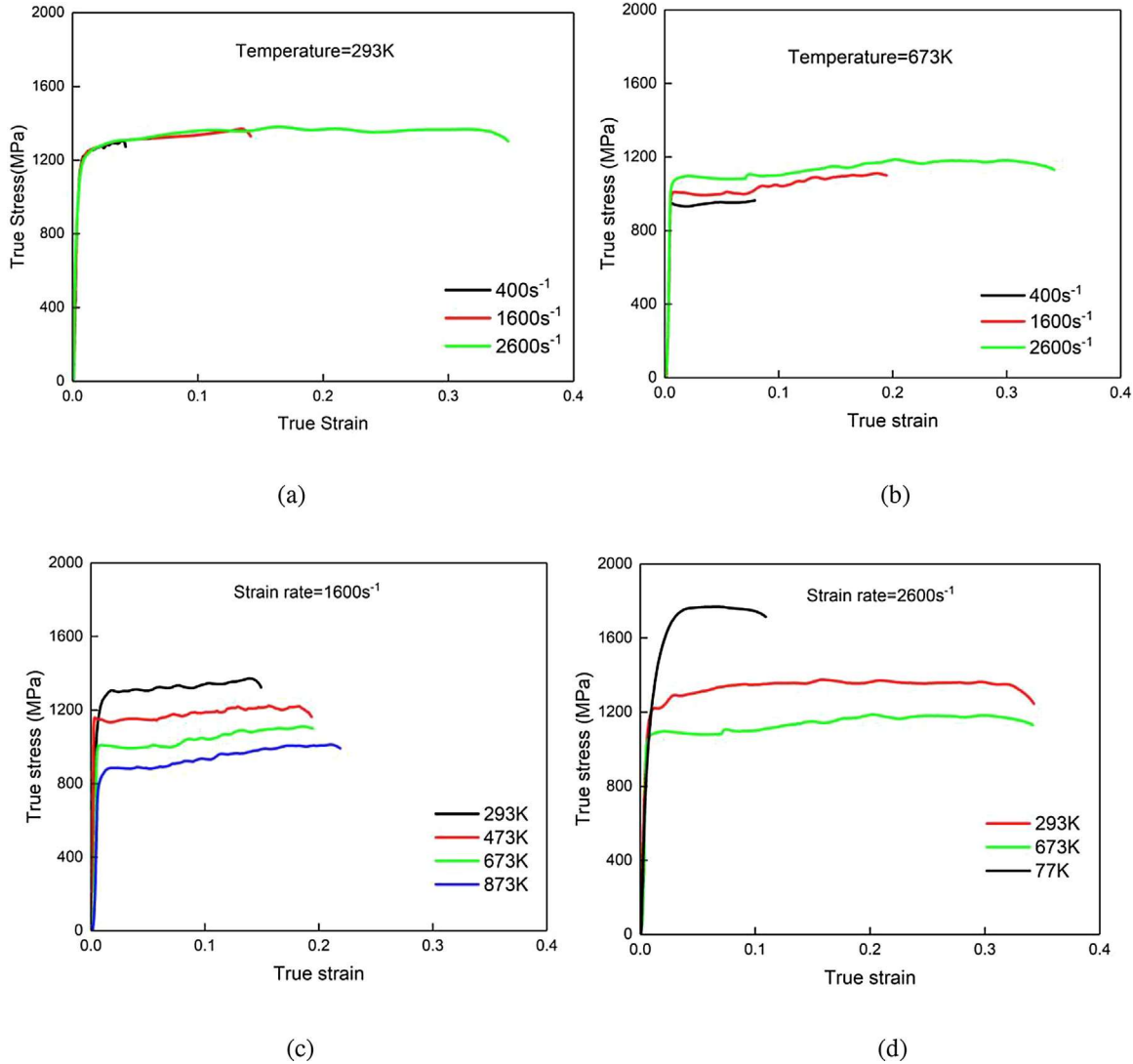


**Fig. 6.** True stress-strain curves of TaNbHfZrTi RHEA samples at different strain rates and temperatures: (a) compressed at room temperature of 293K and strain rates of  $400\text{s}^{-1}$ ,  $1600\text{s}^{-1}$  and  $2600\text{s}^{-1}$ ; (b) compressed at temperature of 673K and strain rates of  $400\text{s}^{-1}$ ,  $1600\text{s}^{-1}$  and  $2600\text{s}^{-1}$ ; (c) compressed at strain rate of  $1600\text{s}^{-1}$  and temperatures of 293K, 473K, 673K and 873K; (d) compressed at strain rate of  $2600\text{s}^{-1}$  and temperatures of 77K, 293K and 673K.

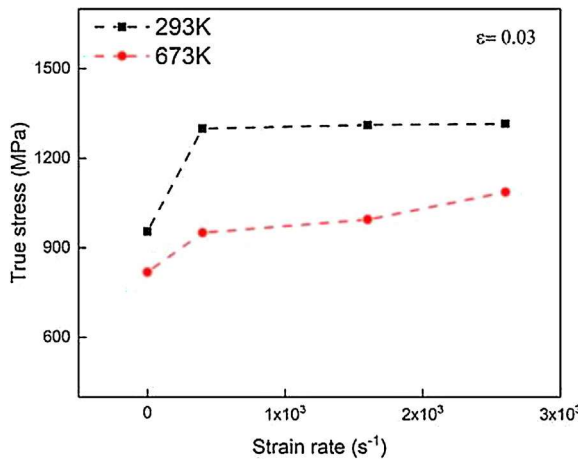


Fig. 7. The flow stress of the TaNbHfZrTi RHEA at 0.03 true plastic strain as a function of strain rate ( $0.001s^{-1} \sim 2600s^{-1}$ ) under temperatures of 293K (black dashed line) and 673K (red dashed line).

**Table. 1**  
Variation of strain rate sensitivity  $\beta$  with temperature.

Strain rate	Temperature	Strain rate sensitivity, $\beta$ (MPa)
$400s^{-1} \sim 2600s^{-1}$	293K	5.34
	673K	75.86

**Table. 2**  
Variation of temperature sensitivity  $\eta_a$  with strain rate.

True strain	Strain rate	Temperature(K)	Temperature sensitivity, $\eta_a$ (MPa/K)
0.03	$1600s^{-1}$	293K-473K	0.83
		473K-673K	0.79
		673K-873K	0.54
	$2600s^{-1}$	77K-293K	2.19
		293K-673K	0.55

tests respectively. The crystal structure of TaNbHfZrTi RHEA is determined by Philips X'pert X-ray diffractometer (XRD) with Cu  $K\alpha$  radiation and the  $2\theta$  range of  $20 \sim 100^\circ$ . The cylindrical specimens before and after compression tests are cut in half along the axial direction and inlaid on epoxy resin to be ground orderly through a series of metallographic sandpaper with different particle sizes ranging from 320 to 3000 mesh. After mechanical grinding and polishing, the specimens are etched with 2ml HF + 2ml HNO<sub>3</sub> + 40ml H<sub>2</sub>O for approximately 2 min. The electrochemical polishing of the primary and the deformed samples are also conducted with 32ml CH<sub>3</sub>OH + 15ml CH<sub>3</sub>(CH<sub>2</sub>)<sub>3</sub>OH + 3ml HClO<sub>4</sub> for about 7-10 sec. The microstructures of TaNbHfZrTi RHEA samples before and after tests are investigated by OM, SEM and EBSD.

## 2.2. Quasi-static compression testing

Quasi-static compression tests under room temperature (293K) and high temperature (673K) are carried out by an electronic universal testing machine equipped with high temperature furnace. The cylindrical specimens with a diameter of 3 mm and a length of 6 mm are deformed at strain rate of  $0.001s^{-1}$ . The temperature is constant during the compression experiment by means of a GW-1200A temperature controller. The true stress and true strain are calculated according to formula (1)-(2)

$$\sigma_T = (1 - \varepsilon)\sigma \quad (1)$$

$$\varepsilon_T = -\ln(1 - \varepsilon) \quad (2)$$

where  $\sigma$  and  $\varepsilon$  are engineering stress and engineering strain, respectively.  $\sigma_T$  and  $\varepsilon_T$  are true stress and true strain, respectively.

## 2.3. Dynamic compression testing

Dynamic compression tests are conducted at strain rates from  $400s^{-1}$  to  $2600s^{-1}$  and temperatures from 77K to 873K through Split Hopkinson Pressure Bar (SHPB) apparatus to obtain the dynamic stress-strain curves. The bars of the SHPB facility are made of 13 mm diameter maraging steel. The length of the incident and transmission pressure bars are both 1000 mm, while the striker bars adopted in the present tests have a length of 250 mm. The cylindrical sample of 5 mm in diameter and 4 mm in length is immersed in liquid nitrogen for about 5 min before the cryogenic temperature dynamic compression experiment to ensure that the sample reached the experimental temperature (77K). When perform tests at elevated temperatures, the sample is heated by a furnace independently. At least three replicates are done for each test condition. The obtained experimental data with good repeatability are averaged and taken as the final result.

The schematic diagram of the SHPB apparatus is shown in Fig. 1. The stress wave pulse signal generated by the impact is captured by the strain gages attached to the middle of the bars. The typical original waveform obtained by the dynamic compression test is depicted in Fig. 2. The Eqs. (3)-(5) for the stress, strain and strain rate of the specimen are based on the one-dimensional elastic stress wave theory. Usually, the strain rate of the sample is not constant during the dynamic compression process, so the average strain rate in the plastic deformation stage is recorded as the dynamic loading strain rate in this study.

$$\sigma_s(t) = \frac{EA_b}{2A_s} \varepsilon_T(t) \quad (3)$$

$$\varepsilon_s(t) = \frac{2C_0}{L} \int_0^t (\varepsilon_I(\tau) - \varepsilon_T(\tau)) d\tau \quad (4)$$

$$\dot{\varepsilon}_s = \frac{2C_0}{L} (\varepsilon_I(t) - \varepsilon_T(t)) \quad (5)$$

where  $\sigma_s$ ,  $\varepsilon_s$  and  $\dot{\varepsilon}_s$  are engineering stress, engineering strain and strain rate of the specimen.  $E$  is the elasticity modulus of the SHPB material.  $A_b$  and  $A_s$  are the cross-sectional areas of the bars and specimen, respectively.  $C_0$  is the elastic wave velocity in pressure bar.  $L$  is the specimen length.  $\varepsilon_I(t)$  and  $\varepsilon_T(t)$  are the incident and transmitted strain pulses, respectively.

## 3. Experimental results and discussion

### 3.1. The suction-assisted cast microstructure

The main diffraction peaks on the XRD pattern of the suction-assisted cast alloy are determined to be BCC phase, which is in consistent with previous studies [11, 29]. Fig. 3 illustrates the indexes of the crystal planes corresponding to the XRD spectra peaks. Typical equiaxed dendritic grains can be clearly seen in backscattered electron image (Fig. 4). As known, the grain size and morphology are depended on the cooling rate of the casting process. A higher cooling rate of the suction-assist casting process in the present study than that of the gravity casting process [11] makes a relatively uniform and smaller grain size of the alloy.

### 3.2. Stress-strain curves

Fig. 5 displays the true plastic stress-strain curves of the compression experiments at different temperatures and strain rates. Apparent strain hardening behavior is found in quasi-static tests. For the dynamic

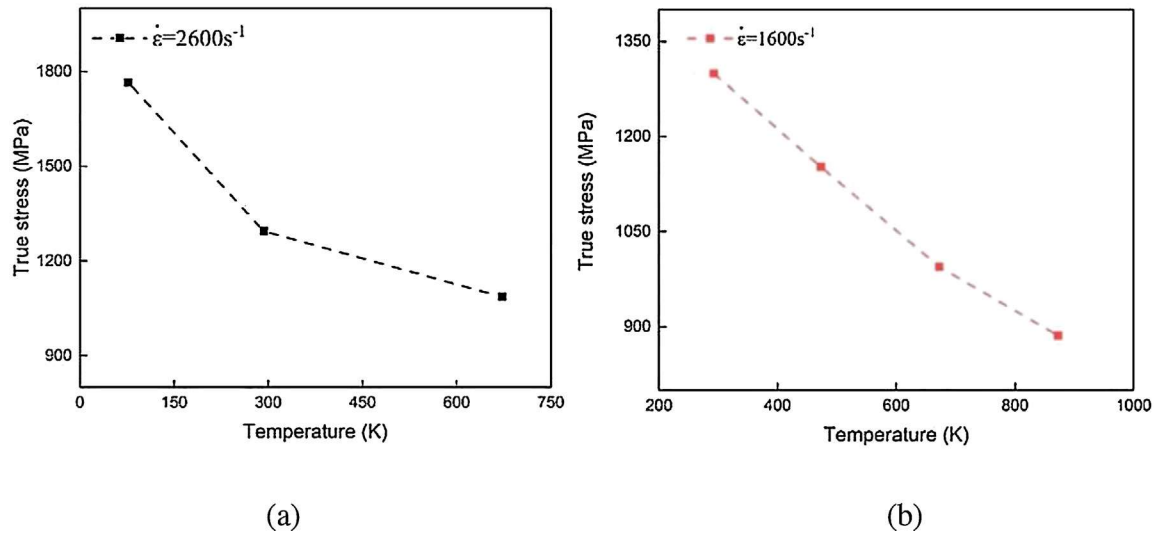


**Fig. 8.** The flow stress of TaNbHfZrTi RHEA at 0.03 true plastic strain as a function of temperature in different strain rates; (a) compressed at strain rate of  $2600 \text{ s}^{-1}$  under temperature from 77K to 673K; (b) compressed at strain rate of  $1600 \text{ s}^{-1}$  under temperature from 293K to 873K.

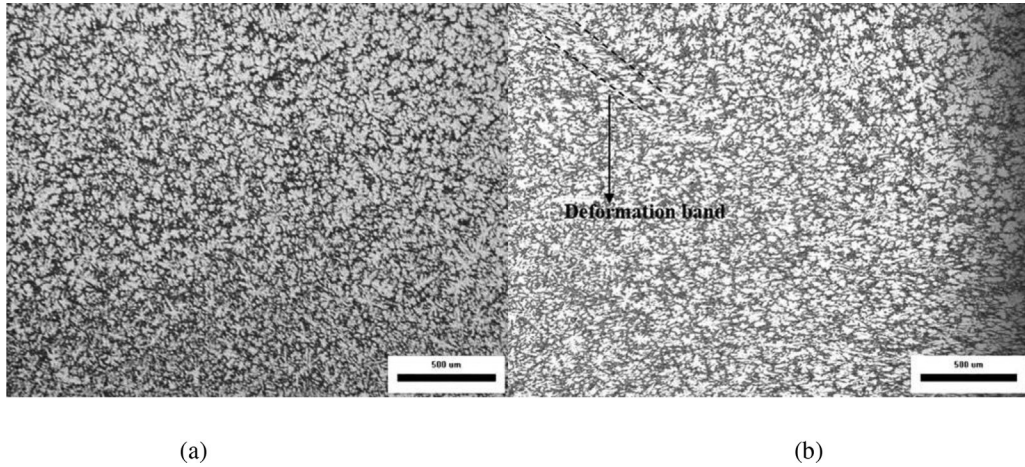


**Fig. 9.** OM images along the longitudinal cross section of TaNbHfZrTi RHEA samples; (a) before quasi-static tests at room temperature; (b) deformation band in the top-left corner of the picture after quasi-static tests at room temperature.

compression tests at 293K, TaNbHfZrTi RHEA exhibits a significant improvement in yield strength with an absence of strain hardening behavior compared with the quasi-static tests. Besides, obvious strain hardening behavior is not found in any dynamic tests at temperatures ranging from 77K to 873K. During the dynamic compression tests, control of the loading time is achieved by the length of the striker bar. As mentioned above, a 250mm length striker is adopted in all the tests. Therefore, both the strain rate and strain increase with increasing the impact speed of the striker.

It can be seen from Fig. 6(a) that the flow stress increases little with increasing the strain rate from  $400 \text{ s}^{-1}$  to  $2600 \text{ s}^{-1}$  at room temperature (293K). In other words, the strain rate effect is observed scarcely at room temperature under the adopted dynamic impact conditions. However, as shown in Fig. 6(b), the flow stress of the TaNbHfZrTi RHEA increases with increasing the strain rate during dynamic impact tests at elevated temperature of 673K, exhibiting apparent strain rate effect. Fig. 6(c) presents that the flow stresses decrease with increasing the temperatures from 293K to 893K at the strain rate of  $1600 \text{ s}^{-1}$ . As known for BCC metals, the flow stress with strong dependence on the temperature is mainly Peierls-Nabarro stress, which belongs to short-range barrier [39, 40]. For the dynamic compression tests under elevated temperatures, thermal energy decreases the height of the barrier effectively, thus lead-

ing to a strength decrease of the TaNbHfZrTi RHEA (Fig. 6(c)). In addition, at the strain rate of  $2600 \text{ s}^{-1}$ , the flow stresses depicted in Fig. 6(d) increase rapidly from about 1294MPa to 1760MPa with decreasing the temperature from room temperature (293K) to liquid nitrogen temperature (77K).

### 3.3. Strain rate and temperature sensitivity

The strain rate sensitivity of TaNbHfZrTi RHEA can be examined by observing the change of flow stress with strain rate. For the true plastic strain of 0.03, the dynamic flow stresses at both room temperature (293K) and elevated temperature (673K) are much higher than the quasi-static flow stresses (Fig. 7). However, at high strain rate range of  $400 \text{ s}^{-1}$  to  $2600 \text{ s}^{-1}$ , the flow stresses at 0.03 true plastic strain remain nearly unchanged. In other words, at room temperature, the TaNbHfZrTi high entropy alloy is strain rate insensitive in the present high strain rate range regime. The dependence of the strain rate effect on the temperature can be studied by calculating the strain rate sensitivity parameters:

$$\beta = \frac{\sigma_2 - \sigma_1}{\ln(\dot{\epsilon}_2/\dot{\epsilon}_1)} \quad (6)$$

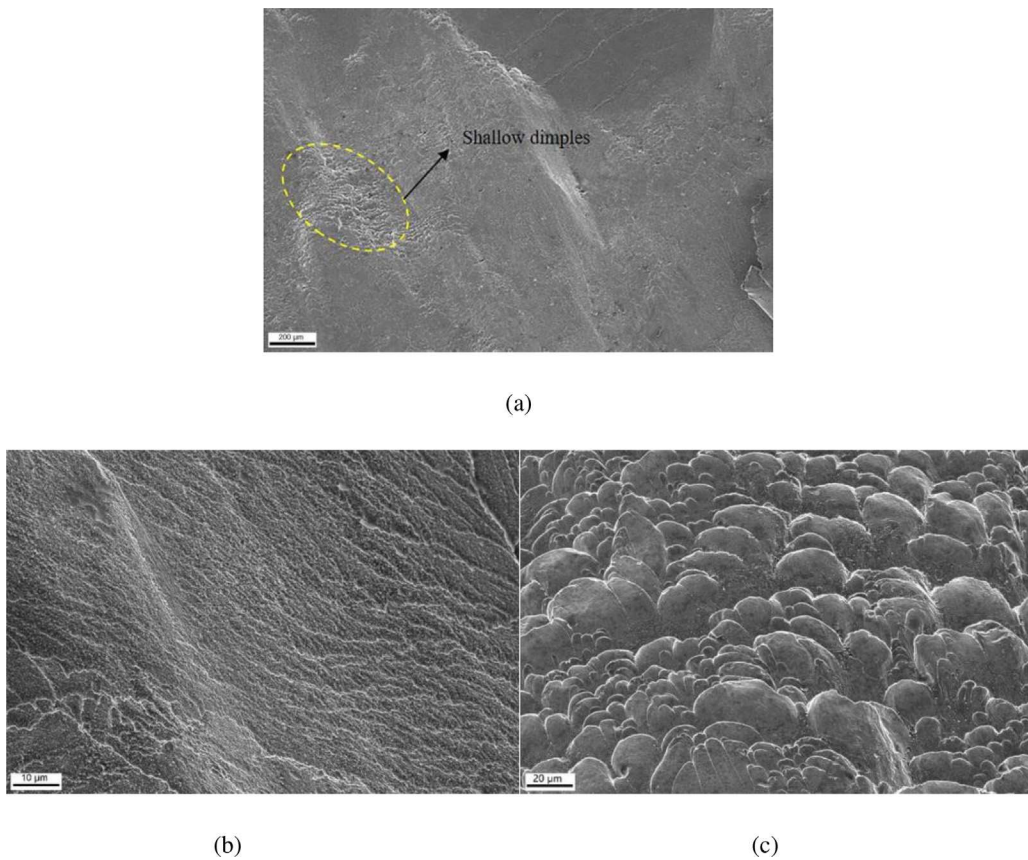


**Fig. 10.** SEM images of the fracture surfaces on the TaNbHfZrTi RHEA samples deformed at strain rate of  $2600\text{s}^{-1}$  under temperature of 77K; (a) relatively flat fracture surface with shallow dimples circled by yellow dashed line; (b) river like patterns on the fracture surface; (c) shallow dimples in high resolution.

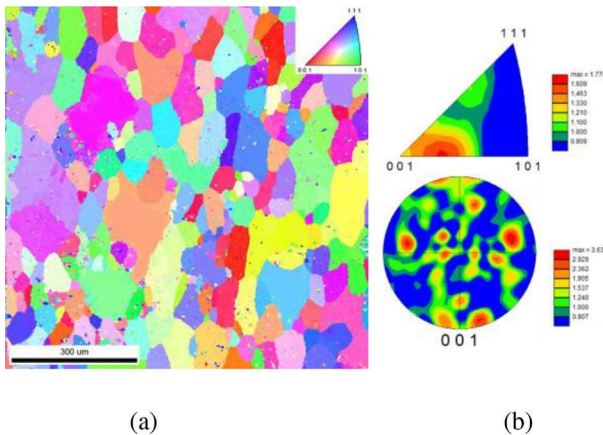


**Fig. 11.** The grain orientation maps by EBSD of the suction-assisted cast TaNbHfZrTi RHEA; (a) grain orientation map with an inset triangle legend and non-indexed dots in grains ; (b) IPF in the upper part and PF in the lower part, apparent preferred grain orientations caused by suction-assisted casting.

where  $\sigma_2$  and  $\sigma_1$  are the compression stresses at different high strain rates of  $\dot{\epsilon}_2$  and  $\dot{\epsilon}_1$ , respectively. The presented strain rate sensitivity parameters in Table 1 demonstrate that the strain rate sensitivity increases significantly as the temperature is increased from 293K to 673K, which indicates an evident strain rate effect.

The variations of flow stresses with the temperatures shown in Fig. 8(a) and (b) demonstrate that the material remains a relatively high strength under elevated temperatures. It is apparent from Fig. 8(a) that liquid nitrogen temperature has a great influence on the increase of flow

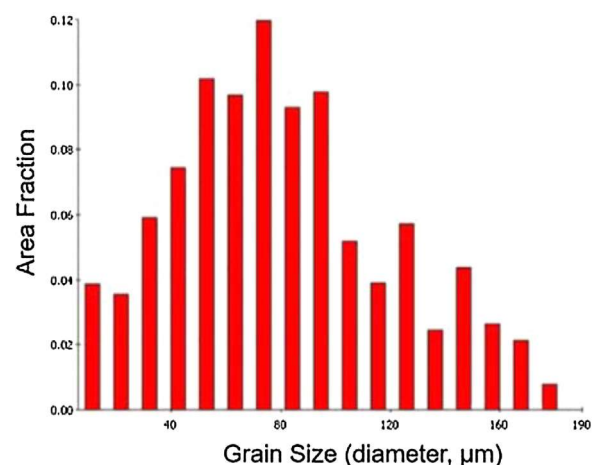


**Fig. 12.** Grain size histogram of the suction-assisted cast TaNbHfZrTi RHEA before compression tests.

stress at strain rate of  $2600\text{s}^{-1}$ . The thermal softening law of materials under high temperature and high strain rate conditions can be explored by temperature sensitivity parameters which are calculated from Eq. (7).

$$\eta_a = \left| \frac{\sigma_2 - \sigma_1}{T_2 - T_1} \right| \quad (7)$$

where  $\sigma_2$  and  $\sigma_1$  are the compression stresses at different high temperatures of  $T_2$  and  $T_1$ , respectively. Table 2 compares the temperature sensitivity of the TaNbHfZrTi RHEA specimens at different strain rates and temperature ranges.

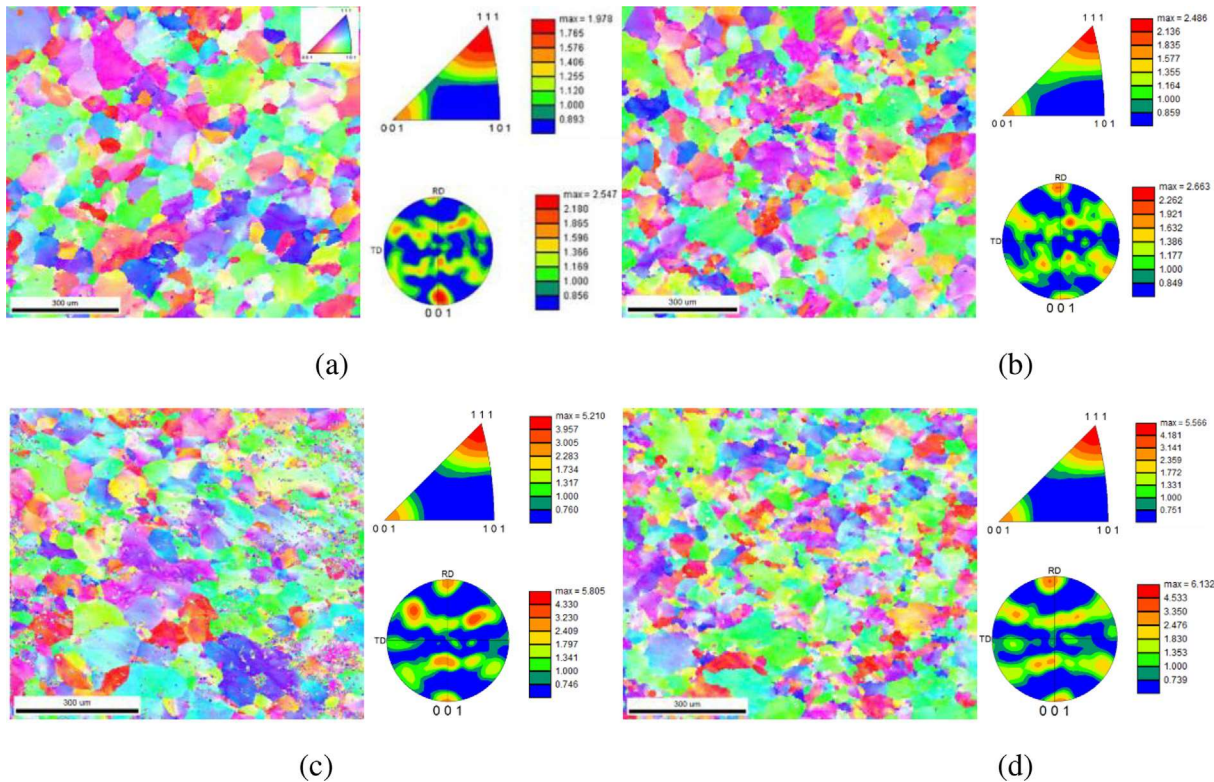


**Fig. 13.** Grain orientation maps, IPFs and PFs of the dynamic compressed TaNbHfZrTi samples at different strain rates and temperatures; (a) sample deformed to a true strain of 0.13 at strain rate of  $1600\text{s}^{-1}$  and temperature of 293K; (b) sample deformed to a true strain of 0.19 at strain rate of  $1600\text{s}^{-1}$  and temperature of 673K; (c) sample deformed to a true strain of 0.33 at strain rate of  $2600\text{s}^{-1}$  and temperature of 293K; (d) sample deformed to a true strain of 0.34 at strain rate of  $2600\text{s}^{-1}$  and temperature of 673K.

According to Table 2, the temperature sensitivity decreases with increasing the temperatures in the range of 293K~873K. Overall, the results presented in Table 2 illustrate that temperature has a significant effect on the mechanical response of TaNbHfZrTi RHEA under high strain rates. From the above analysis, it can be concluded that there exist the coupled effects of strain rate and temperature on microstructure evolution of TaNbHfZrTi RHEA. It is known that dislocations can overcome Peierls-Nabarro barriers by thermal energy effect on the vibration of atoms during quasi-static compression [40]. Viscous-drag on the dislocation glide can be generated by the interaction of dislocations with phonons. Dislocation velocities at quasi-static conditions are so low that phonon drag plays a negligible role on dislocation motion. However, under dynamic compression condition there is less time available to overcome the barrier and the thermal energy will be less effective [35, 40]. Therefore, phonon drag effects on dislocation motion can't be ignored anymore, and a quick rise of the yield stress is required to make dislocation velocities comparable to the loading strain rate. Hence, the strain rate hardening phenomenon appears in the present tests (see Fig. 5 and Fig. 7). Nevertheless, it should be noted that the flow stress of TaNbHfZrTi RHEA varied little during dynamic compression under room temperature. The reason for the insensitivity of the strain rate effect ( $400\text{s}^{-1}$  to  $2600\text{s}^{-1}$ ) at room temperature may due to an identical effect of the viscous-drag under the dynamic loading conditions. In other words, the variation of the strain rate in the present dynamic regime is too small to strengthen the viscous-drag effect and further influence the flow stress. However, as the dislocation drag is caused by the interaction with phonons, the influence of viscous-drag increases with the temperature [41, 42]. Therefore, under the impact of the elevated temperature (673K), the strain rate sensitivity of TaNbHfZrTi is enhanced in the present dynamic tests (see Fig. 6b and Fig. 7).

### 3.4. Microstructure analysis

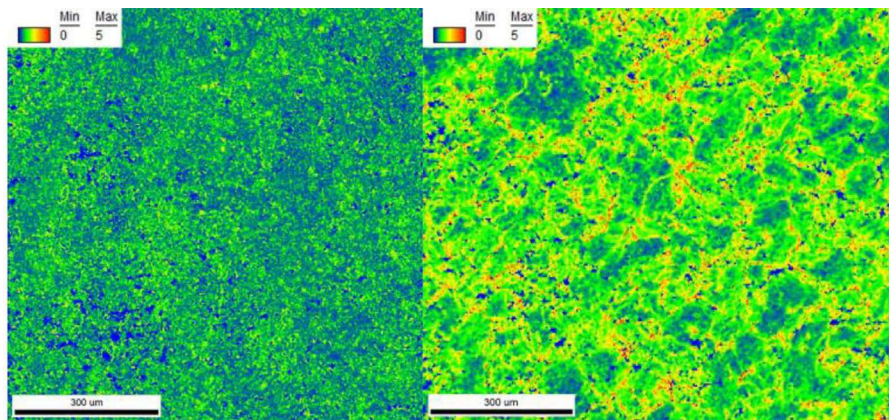
#### 3.4.1. Metallographic examinations under quasi-static tests

Metallographic examinations of the samples before and after quasi-static compression at 293K are shown in Fig. 9(a) and (b), respectively. The compressed sample with a true plastic strain of 0.3 reveals a deformation band which can be seen at the top left corner of Fig. 9(b). However, except for the slight deformation band, the rest of the microstructure in Fig. 9(b) displays a stable state and homogeneous deformation, which suggests a potential good ductility.

#### 3.4.2. Microstructure characterization under dynamic tests

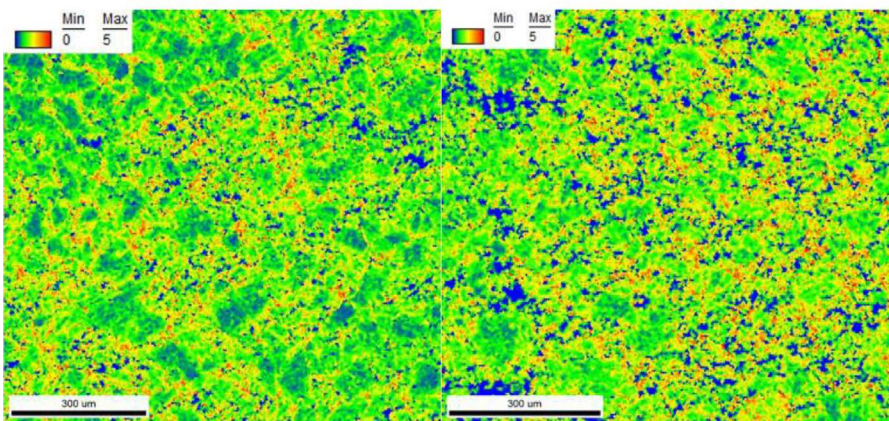
Dynamic shear failure occurs in the TaNbHfZrTi RHEA at a true strain of about 0.1 due to the decrease of plasticity under liquid nitrogen temperature at the strain rate of  $2600\text{s}^{-1}$ . In Fig. 10(a), the fracture morphology of the sample examined by SEM has a relatively flat surface except for a small part of shallow dimple patterns, suggesting a limited ductility under liquid nitrogen temperature. In addition, river patterns representing brittle fracture feature on the fracture surfaces are also observed (see Fig. 10(b)). The shallow dimples marked yellow dashed line in Fig. 10(a) are clearly presented by a higher magnification image in Fig. 10(c). The shear dimples shown in Fig. 10(c) are much shallower than those shown by SEM images reported by O.N. Senkov et al. [30, 33], which is attributed to the high strain rate and low temperature conditions. Overall, the suction-assisted cast TaNbHfZrTi RHEA appears to have a mixture of brittle and ductile fracture mechanism under the low temperature (77K) impact loading condition.

Fig. 11(a) presents the grain orientation distribution map of the suction-assisted cast TaNbHfZrTi RHEA sample before compression tests. The step size for EBSD is  $4\mu\text{m}$  and the legend to the grain orientation map is the inset triangle shown in Fig. 11(a). Red, green and blue represent the three crystal directions [001], [101] and [111] of the



(a)

(b)



(c)

(d)

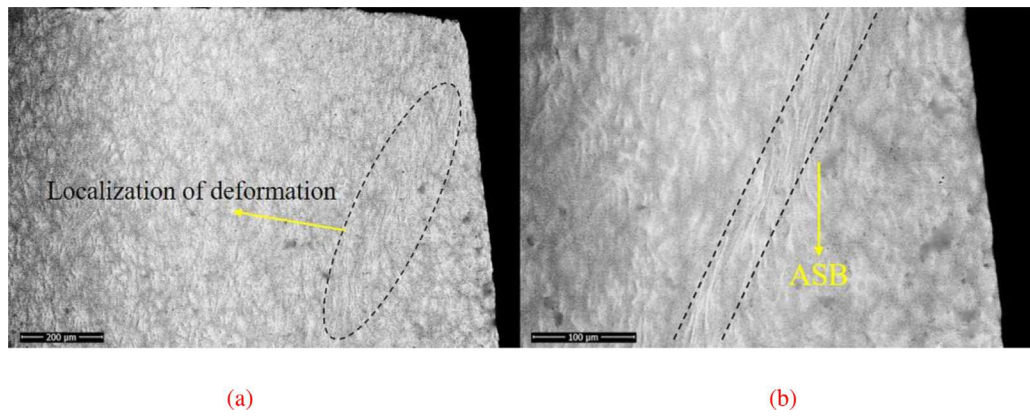


**Fig. 15.** SEM-BSE images of the shear localization region at true strain of 0.33 in the strain rate of  $2600\text{s}^{-1}$  and temperature of 293K; (a) elongated grains in the deformation localization area circled by black dashed line; (b) magnification image of ASB in the deformation localization region in (a).

grains parallel to the cross-sectional direction. Compared to the random crystallographic texture of the as-cast TaNbHfZrTi RHEA [26], the corresponding pole figure (PF) and inverse pole figure (IPF) of (001) shown in Fig. 11(b) denote a rather preferred crystallographic texture of the RHEA due to the suction-assisted casting process. According to EBSD analysis, the initial suction-assisted cast TaNbHfZrTi RHEA has a grain size range of 10~180 μm with an average value of about 82 μm, and the grain size histogram is also depicted in Fig. 12. The average grain size

of the suction-assisted cast TaNbHfZrTi RHEA is much smaller than that of the gravity casting process due to a high cooling rate.

The TaNbHfZrTi samples after dynamic compression at different strain rates ( $1600\text{s}^{-1}$  and  $2600\text{s}^{-1}$ ) and temperatures (293K and 673K) are investigated by EBSD with a scanning step size of  $4\mu\text{m}$ . The grain orientation maps obtained by the EBSD analysis are shown in Fig. 13(a)~(d). The inset triangle legend shown in Fig. 13(a) is the same as that inset in Fig. 11(a). The three crystallographic orientations

**Table. 3**  
The calculated parameters of the modified J-C model.

Parameter	A	B	n	C <sub>1</sub>	C <sub>2</sub>	a	b <sub>1</sub>	b <sub>2</sub>
Value	910	1092	0.82	0.024	-0.075	0.811	8.023×10 <sup>-5</sup>	5.886×10 <sup>-8</sup>

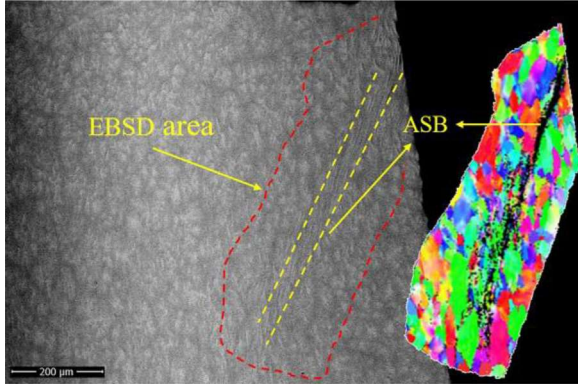


**Fig. 16.** SEM-BSE image with EBSD area marked by red dashed line and ASB marked by yellow dashed line and the corresponding grain orientation distribution map. TaNbHfZrTi sample deformed to a true strain of 0.34 in the strain rate of 2600 s<sup>-1</sup> and temperature of 673K.

parallel to the loading axis are also represented by three colors. From the grain orientation distribution maps shown in Fig. 13(a)~(d), colors in the grains are not as homogeneous as the map shown in Fig. 11(a), which is attributed to the plastic deformation in dynamic tests. IPFs and PFs in Fig. 13(a)~(d) give the specific results of the texture evolution. The compressed grains mainly exhibit blue and red colors consisting of gradations inside, which demonstrates that the deformed grains preferentially have strong <111> and relatively weak <001> orientations and parallel to the compression axial. For BCC metals and alloys deformed in compression, the <111> and <001> orientations parallel to the compression axial are known as the typical plastic deformation texture. As is shown in Fig. 13(a)~(d), it worth noting that the maximum grain orientation intensity of IPFs increases from 1.978 to 5.566 with increasing the strain rate from 1600 s<sup>-1</sup> to 2600 s<sup>-1</sup> and the temperature from 293K to 673K. The scanning area in Fig. 13(a)~(d) are all located on the cen-

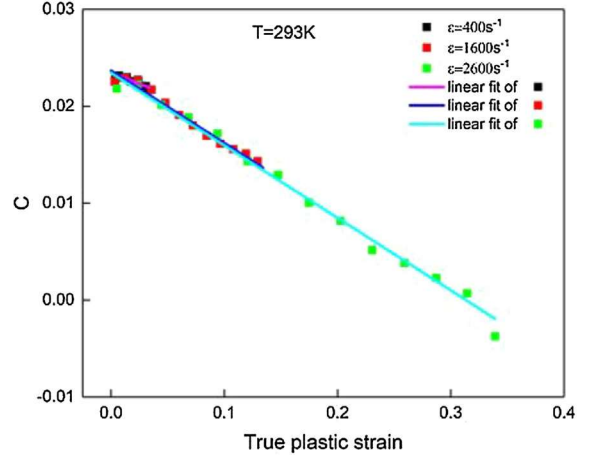


**Fig. 17.** Variation of C with strain and strain rate (400 s<sup>-1</sup>, 1600 s<sup>-1</sup> and 2600 s<sup>-1</sup>) at 293K.

tral part of the longitudinal cross section of the deformed sample. It can be easily seen from Fig. 13(a)~(d) that both localized deformation and adiabatic shear bands (ASB) are not found in the scanning areas.

The Kernel Average Misorientation (KAM) maps of the samples after dynamic compression at different strain rates and temperatures are plotted in the light of the third nearest neighbor with a maximum misorientation angle of 5°, respectively (see Fig. 14(b), (c) and (d)). Fig. 14(a) shows the KAM map of the initial sample without deformation. The given KAM maps in Fig. 14(a)~(d) demonstrate the BCC lattice rotations of the TaNbHfZrTi RHEA which happen most likely due to the dislocations stored in the lattice. The red and yellow colors shown in Fig. 14(b) and (c) indicate a high value of dislocation density due to plastic deformation. It can also be seen from Fig. 14(b), (c) and (d) that the KAM values increase with increasing the strain rate and temperature,

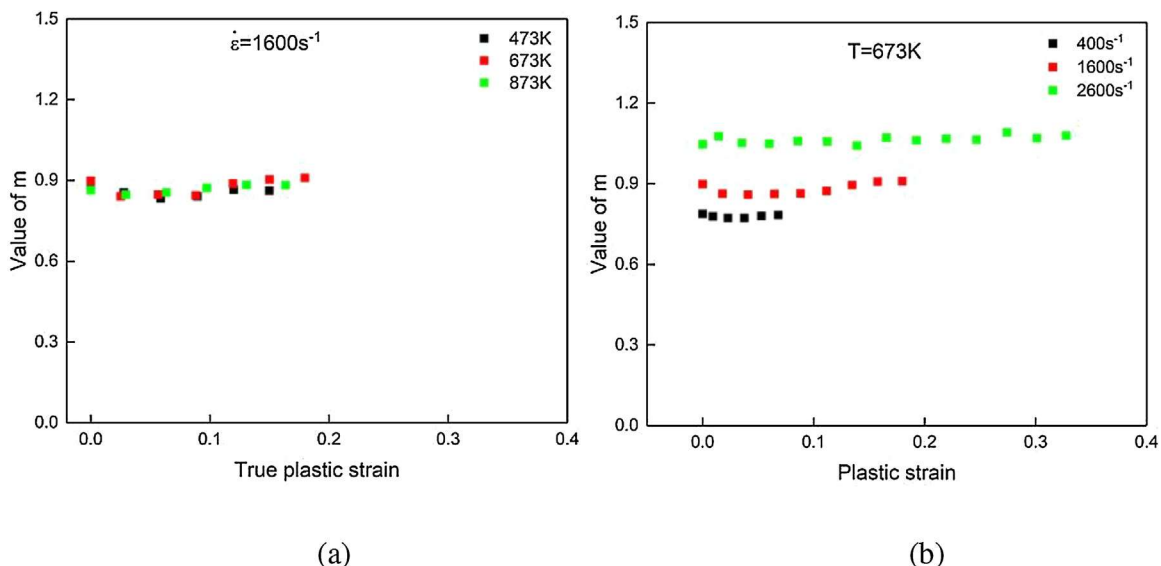


**Fig. 18.** (a) Variation of m with temperature at strain rate of 1600 s<sup>-1</sup>; (b) Variation of m with strain rate at temperature of 673K.

which is in accordance with the grain orientation evolution depicted in Fig. 11 and Fig. 13. It is well known that the free energy of solid solution phases is lowered by the higher mixing entropy of HEAs, which facilitates the formation of stable multicomponent solid solution, especially at elevated temperatures [8]. Moreover, the properties of TaNbHfZrTi RHEA are also strengthened by the severe lattice distortion which impedes the dislocation movement and contributes to the prominent solid solution strengthening [10]. The homogeneously deformed microstructures shown in Fig. 13 and Fig. 14 suggest a pronounced solid solution stability of the TaNbHfZrTi RHEA at high strain rates and high temperatures. In conventional metal alloys with single BCC phase, the propagation of screw dislocations is usually controlled by Peierls stress and the phonon drag mechanism. The motion of screw dislocations in the BCC RHEAs may further be restricted by the inherent lattice distortion, which leading to high strength and low ductility of many refractory BCC HEAs. However, the intrinsic ductility of BCC HEAs is also relative to Valence Electron Concentration (VEC), and RHEAs at VEC  $\leq 4.4$  are ductile [43]. From the point view of VEC in BCC HEAs, TaNbHfZrTi RHEA at VEC  $\approx 4.3$  (see Fig. 9 in the paper by Chen et al. [4]) demonstrates a good ductility among the RHEAs. Moreover, the reduction in the average grain size from  $\sim 200\mu\text{m}$  in the as-cast state [26] to  $\sim 82\mu\text{m}$  in the current suction-assisted cast state has apparently enhanced the critical strain of the shear localization (see Fig. 15 and Fig. 16). Similar enhancement to the fracture strain of TaNbHfZrTi alloy by the grain size reduction is also stated by Praveen et al. [44] and Juan et al. [45].

ASBs are clearly seen in the SEM-BSE images shown in Fig. 15 and Fig. 16. It should be noted that ASB formation regions are in the corner of the longitudinal cross section of the deformed sample, where are easy to form stress concentration. The ASBs in Fig. 15 and Fig. 16 are conveniently estimated to be tens of microns by the ruler of the SEM-BSE image. Because a high resolution can cause a high sensitivity to drift, a scanning step size of  $1.5\mu\text{m}$  is adopted in the adiabatic shear band region to optimize the resolution of EBSD without increasing too much acquisition time. The grain orientation map presented in Fig. 16 corresponds to the region circled by the red dashed lines. The color legend of the grain orientation map is identical to the inset triangle legend in Fig. 13(a). The black band (un-indexed pixels) in the grain orientation map is identified to be ASB. The grains in the vicinity of ASB are severely elongated and rotated, which suggest a large plastic deformation before ASB initiation. The ASB in Fig. 16 with an approximately length of  $700\mu\text{m}$  does not go through the sample apparently. Therefore, the suction-assisted cast TaNbHfZrTi RHEA possesses excellent plasticity at high strain rate compression and temperature of 673K. It should be noted that deformation twinning was not occurred even at the intense shear localization region under the highly applied stress through direct impact Hopkinson bar test [26]. Additionally, in the grain orientation maps shown in Fig. 13 (a)-(d) and Fig. 16 deformation twinning is not found either. Therefore, the present tests results demonstrate that the dominated deformation mechanism for suction-assisted cast TaNbHfZrTi RHEA is mainly attributed to the thermally activated screw dislocation at quasi-static condition and the phonon drag controlled screw dislocation motion at high strain rates and high temperatures.

#### 4. The modified J-C model

J-C model is widely used to describe the stress-strain relationship of metal materials under extreme conditions. However, the coupled effect of strain, strain rate and temperature on the deformation of the TaNbHfZrTi RHEA is found during the dynamic compression tests. A modified J-C model is established in the following section, which takes the coupled effects of the factors mentioned above into consideration.

According to the original J-C model, the flow stress can be written as:

$$\sigma = (A + B\epsilon^n)(1 + C \ln \dot{\epsilon}^*) \left(1 - \left(\frac{T - T_r}{T_m - T_r}\right)^m\right) \quad (8)$$

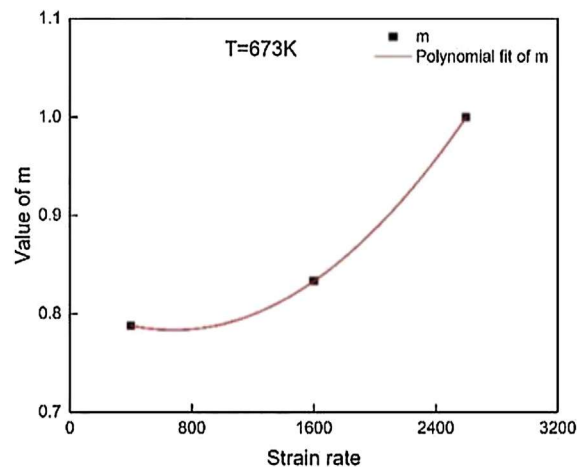


Fig. 19. Relationship between  $m$  and strain rate at temperature of 673K.

where  $\sigma$  and  $\epsilon$  are flow stress and true plastic strain, respectively.  $A$ ,  $B$ ,  $C$ ,  $n$  and  $m$  are constants need to be determined.  $\dot{\epsilon}^* = \dot{\epsilon}/\dot{\epsilon}_0$  is the equivalent strain rate.  $\dot{\epsilon}$  is the true plastic strain rate. The reference strain rate  $\dot{\epsilon}_0$  is  $0.001\text{s}^{-1}$  and the reference temperature  $T_r$  and melting temperature  $T_m$  are 293K and 2523K [16], respectively.

Based on the quasi-static tests data,  $A$ ,  $B$  and  $n$  are calculated to be 910, 1092 and 0.82, respectively. For the high strain rates experiments at room temperature, the first two terms in Eq. (8) can be written as

$$\frac{\sigma}{A + B\epsilon^n} - 1 = C \ln \dot{\epsilon}^* \quad (9)$$

For each true plastic strain rate,  $\dot{\epsilon}^*$  is a constant. Substitute the values of the flow stress and the corresponding true plastic strain at different stain rates into Eq. (9) to get a series values of  $C$ . As is shown in Fig. 17,  $C$  varies with strain at different strain rates and there is an approximate linear relationship between strain and  $C$ .

In order to get accurate constitutive parameter,  $C$  can be improved to a linear function of true plastic strain, see Eq. (10)

$$C = C_1 + C_2\epsilon \quad (10)$$

$C_1$  and  $C_2$  can be identified from the intercept and the slope of the fitted line.

Parameter  $m$  is determined by the dynamic tests at elevated temperatures. The original J-C model can be written as:

$$1 - \frac{\sigma}{(A + B\epsilon^n)(1 + C \ln \dot{\epsilon}^*)} = T^{*m} \quad (11)$$

The values of  $m$  can be obtained by taking a logarithm transformation of Eq. (11). Fig. 18(a) shows the variation of  $m$  with true plastic strain at strain rate of  $1600\text{s}^{-1}$  under different elevated temperatures (473K~873K), while, Fig. 18(b) displays the variation of  $m$  with true plastic strain at different strain rates under the temperature of 673K. From the comparison of Fig. 18(a) and (b), it can be found that  $m$  is independent on temperature but is dependent on strain rate under elevated temperatures.

The values of  $m$  in Fig. 18 (b) are averaged respectively and then plotted in Fig. 17. To clarify the relationship between  $m$  and strain rate under elevated temperatures, a polynomial fitting is adopted, see Fig. 19.

Thus, the modified parameter  $m$  can be expressed as following polynomial equation:

$$m = a + b_1\dot{\epsilon} + b_2\dot{\epsilon}^2 \quad (12)$$

Finally, the improved J-C model is as follows:

$$\sigma = [A + B(\epsilon)^n][1 + (C_1 + C_2)\epsilon \ln \dot{\epsilon}^*] \left[1 - (T^*)^{(a+b_1\dot{\epsilon}+b_2\dot{\epsilon}^2)}\right] \quad (13)$$

All the calculated parameters are listed in Table. 3.

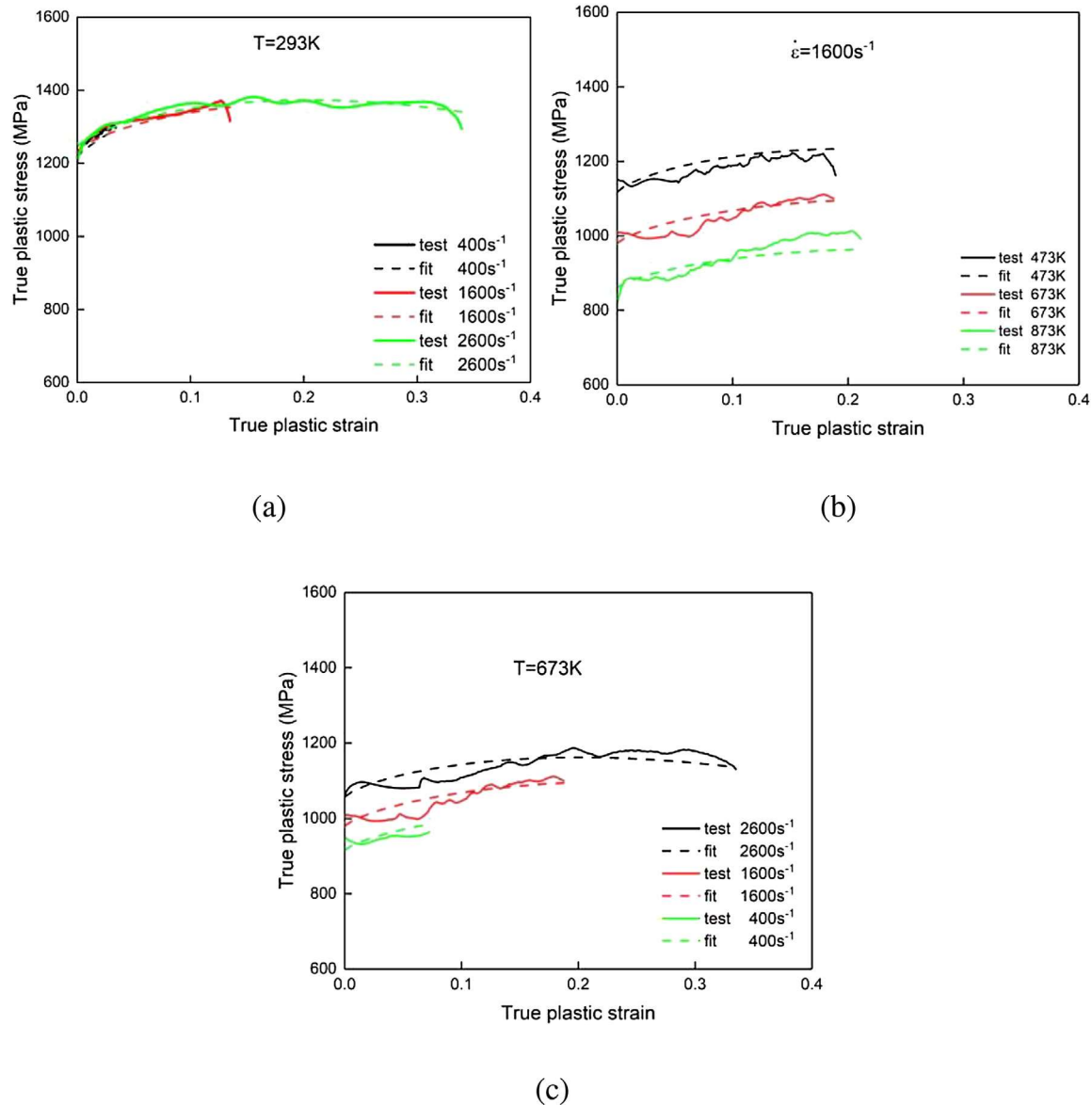


**Fig. 20.** Comparison between the experimental curves and the model predictions: (a) different strain rates of  $400\text{s}^{-1}$ ,  $1600\text{s}^{-1}$  and  $2600\text{s}^{-1}$  at  $293\text{K}$ ; (b) different high temperatures of  $473\text{K}$ ,  $673\text{K}$  and  $873\text{K}$  at  $1600\text{s}^{-1}$ ; (c) different strain rates of  $2600\text{s}^{-1}$ ,  $1600\text{s}^{-1}$  and  $400\text{s}^{-1}$  at  $673\text{K}$ .

The curves of model predictions and the experimental results at different strain rates and elevated temperatures are illustrated in Fig. 20(a)–(c).

It can be observed that the fitting values matched well the experimental results, which indicates that the modified J-C model can be used to exactly predict the dynamic mechanical behaviors of the TaNbHfZrTi RHEA.

## 5. Conclusions

The mechanical behaviors of the suction-assisted cast TaNbHfZrTi RHEA at different strain rates under liquid nitrogen temperature and elevated temperatures are investigated systematically. The prior and post observations on the microstructures offer the insight into the texture evolution and fracture mechanism at the microscopic level. Some conclusions are drawn as follows:

- 1 The TaNbHfZrTi RHEA with high yield strength under liquid nitrogen temperature ( $77\text{K}$ ) and high strain rate ( $2600\text{s}^{-1}$ ) has a fracture morphology exhibiting the co-existence of ductile and brittle fracture mechanism.
- 2 Excellent dynamic compression properties at high temperatures have been found for the TaNbHfZrTi RHEA. Elevated temperature promotes the strain rate hardening of the TaNbHfZrTi RHEA attributed to the intensification of viscous-drag controlled dislocation motion in dynamic tests.
- 3 The microstructures of the suction-assisted cast TaNbHfZrTi RHEA remain homogeneous after large plastic deformation at high strain rates and elevated temperatures, demonstrating remarkable high temperature stability and excellent plasticity.

## Declaration of Competing Interest

None

## Acknowledgements

The authors acknowledge the financial support of the National Key R and D Program of China (2016YFC0801200), the National Natural Science Foundation of China (11672043, 11972092, 11802028, 11732003), the Project of China Postdoctoral Science Foundation (2018M640072), the opening project of State Key Laboratory for Strength and Vibration of Mechanical Structures (SV2019-KF-02) and the Project of State Key Laboratory of Explosion Science and Technology (YBKT18-07, KFJJ19-12M).

## References

- [1] Senkov ON, Wilks GB, Miracle DB, Chuang CP, Liaw PK. Refractory high-entropy alloys. *Intermetallics* 2010;18:1758–65.
- [2] Yeh JW, Chen SK, Lin SJ, Gan JY, Chin TS, Shun TT, Tsau CH, Chang SY. Nanosstructured high-entropy alloys with multiple principal elements: novel alloy design concepts and outcomes. *Adv. Eng. Mater* 2004;6:299–303.
- [3] E JNGPICKERING, alloys High-entropy: a critical assessment of their founding principles and future prospects. *Int. Mater. Rev* 2016;3:183–202.
- [4] Chen J, Zhou X, Wang W, Liu B, Lv Y, Yang W, Xu D, Liu Y. A review on fundamental of high entropy alloys with promising high-temperature properties, *J. Alloy. Compd.* 2018;760:15–30.
- [5] Cao Y, Ni S, Liao X, Song M, Zhu Y. Structural evolutions of metallic materials processed by severe plastic deformation. *Mater. Sci. Eng. R-Rep* 2018;133:1–59.
- [6] Gludovatz B, George EP, Ritchie RO. Processing, microstructure and mechanical properties of the crmnfeconi high-entropy alloy. *Jom-US* 2015;67:2262–70.
- [7] Miracle DB, Senkov ON. A critical review of high entropy alloys and related concepts. *Acta Mater* 2017;122:448–511.
- [8] Tsai M, Yeh J. High-entropy alloys: a critical review. *Mater Res Lett* 2014;2:107–23.
- [9] Ye YF, Wang Q, Lu J, Liu CT, Yang Y, alloy High-entropy. challenges and prospects. *Mater. Today* 2016;19:349–62.
- [10] Zhang Y, Zuo TT, Tang Z, Gao MC, Dahmen KA, Liaw PK, Lu ZP. Microstructures and properties of high-entropy alloys. *Prog. Mater. Sci.* 2014;61:1–93.
- [11] Senkov ON, Scott JM, Senkova SV, Miracle DB, Woodward CF. Microstructure and room temperature properties of a high-entropy TaNbHfZrTi RHEA, *J. Alloy. Compd.* 2011;509:6043–8.
- [12] Wang W, Wang W, Wang S, Tsai Y, Lai C, Yeh J. Effects of Al addition on the microstructure and mechanical property of AlxCrCoFeNi high-entropy alloys. *Intermetallics* 2012;26:44–51.
- [13] Sistla HR, Newkirk JW, Frank Liou F. Effect of Al/Ni ratio, heat treatment on phase transformations and microstructure of AlxFeCoCrNi2-x ( $x=0.3, 1$ ) high entropy alloys, *Mater. Des* 2015;81:113–21.
- [14] Chen J, Niu P, Liu Y, Lu Y, Wang X, Peng Y, Liu J. Effect of Zr content on microstructure and mechanical properties of AlCoCrFeNi high entropy alloy. *Mater. Des* 2016;94:39–44.
- [15] Lilenstein L, Couzinié JP, Perrière L, Bourgon J, Emery N, Guillot I. New structure in refractory high-entropy alloys. *Mater. Lett* 2014;132:123–5.
- [16] Gao MC, Carney CS, Doğan ÖN, Jablonksi PD, Hawk JA, Alman DE. Design of refractory high-entropy alloys. *Jom-US* 2015;67:2653–69.
- [17] Senkov ON, Miracle DB, Chaput KJ, Couzinie J. Development and exploration of refractory high entropy alloys—a review, *J. Mater. Res* 2018;1–37.
- [18] Chen SY, Tong Y, Tseng KK, Yeh JW, Poplawsky JD, Wen JG, Gao MC, Kim G, Chen W, Ren Y, Feng R, Li WD, Liaw PK. Phase transformations of HfNbTaTiZr high-entropy alloy at intermediate temperatures. *Sci. Mater* 2019;158:50–6.
- [19] Chien-Chang Juan A KAW. Solution strengthening of ductile refractory HfMoxNbTa-TiZr high-entropy alloys. *Mater. Lett* 2016;175:284–7.
- [20] Čížek J, Haušild P, Cieslar M, Melikhova O, Vlasák T, Janeček M, Král R, Harcuba P, Lukáč F, Zýka J, Málek J, Moon J, Kim HS. Strength enhancement of high entropy alloy HfNbTaTiZr by severe plastic deformation, *J. Alloy. Compd.* 2018;768:924–37.
- [21] Couzinié JP, Dirras G, Perrière L, Chauveau T, Leroy E, Champion Y, Guillot I. Microstructure of a near-equimolar refractory high-entropy alloy. *Mater. Lett* 2014;126:285–7.
- [22] Senkov ON, Scott JM, Senkova SV, Meisenkothen F, Miracle DB, Woodward CF. Microstructure and elevated temperature properties of a refractory TaNbHfZrTi RHEA, *J. Mater. Sci.* 2012;47:4062–74.
- [23] Stepanov ND, Yurchenko NY, Zherebtsov SV, Tikhonovsky MA, Salishchev GA. Aging behavior of the HfNbTaTiZr high entropy alloy. *Mater. Lett* 2018;211:87–90.
- [24] Han ZD, Chen N, Zhao SF, Fan LW, Yang GN, Shao Y, Yao KF. Effect of Ti additions on mechanical properties of NbMoTaW and VNbMoTaW refractory high entropy alloys. *Intermetallics* 2017;84:153–7.
- [25] Fazakas É, Zadorozhny V, Varga LK, Inoue A, Louzguine-Luzgin DV, Tian F, Vitos L. Experimental and theoretical study of Ti20Zr20Hf20Nb20X20 (X=V or Cr) refractory high-entropy alloys. *Int. J. Refract. Met. Hard Mat* 2014;47:131–8.
- [26] Dirras G, Couque H, Lilenstein L, Heczel A, Tingaud D, Couzinié JP, Perrière L, Gubicza J, Guillot I. Mechanical behavior and microstructure of Ti20Hf20Zr20Ta20Nb20 high-entropy alloy loaded under quasi-static and dynamic compression conditions. *Mater. Charact* 2016;111:106–13.
- [27] Dirras G, Gubicza J, Heczel A, Lilenstein L, Couzinié JP, Perrière L, Guillot I, Hocini A. Microstructural investigation of plastically deformed Ti20Zr20Hf20Nb20Ta20 high entropy alloy by x-ray diffraction and transmission electron microscopy. *Mater. Charact* 2015;108:1–7.
- [28] Dirras G, Lilenstein L, Djemia P, Laurent-Brocq M, Tingaud D, Couzinié JP, Perrière L, Chauveau T, Guillot I. Elastic and plastic properties of as-cast equimolar TiHfZrTaNb high-entropy alloy. *Mater. Sci. Eng. A* 2016;654:30–8.
- [29] Larianovsky N, Katz-Demyanetz A, Eshed E, Regev M. Microstructure, tensile and creep properties of Ta20Nb20Hf20Zr20Ti20 high entropy alloy. *Materials* 2017;10:883.
- [30] Senkov ON, Semiatin SL. Microstructure and properties of a refractory high-entropy alloy after cold working. *J. Alloy. Compd.* 2015;649:1110–23.
- [31] Zou Y, Maiti S, Steurer W, Spolenak R. Size-dependent plasticity in an Nb25Mo25Ta25W25 refractory high-entropy alloy. *Acta Mater* 2014;65:85–97.
- [32] Senkov ON, Wilks GB, Scott JM, Miracle DB. Mechanical properties of Nb25Mo25Ta25W25 and V20Nb20Mo20Ta20W20 refractory high entropy alloys. *Intermetallics* 2011;19:698–706.
- [33] Senkov ON, Pilchak AI, Semiatin SL. Effect of cold deformation and annealing on the microstructure and tensile properties of a HfNbTaTiZr refractory high entropy alloy. *Metall. Mater. Trans. A* 2018;49:2876–92.
- [34] Li Z, Zhao S, Alotaibi SM, Liu Y, Wang B, Meyers MA. Adiabatic shear localization in the CrMnFeCoNi high-entropy alloy. *Acta Mater* 2018;151:424–31.
- [35] Kumar N, Ying Q, Nie X, Mishra RS, Tang Z, Liaw PK, Brennan RE, Doherty KJ, Cho KC. High strain-rate compressive deformation behavior of the Al0.1CrFeCoNi high entropy alloy. *Mater. Des* 2015;86:598–602.
- [36] Jiao ZM, Ma SG, Chu MY, Yang HJ, Wang ZH, Zhang Y, Qiao JW. Superior mechanical properties of AlCoCrFeNiTi high-entropy alloys upon dynamic loading, *J. Mater. Eng. Perform.* 2016;25:451–6.
- [37] Michael Pereira BALJ. Effects of material microstructure on blunt projectile penetration of a nickel-based super alloy. *Int. J. Impact Eng* 2009;36:1027–43.
- [38] Michael Pereira BALJ. Effects of heat treatment on the ballistic impact properties of Inconel 718 for jet engine fan containment applications. *Int. J. Impact Eng* 2001;25:715–33.
- [39] Taylor G, Taylor G. Thermally-activated deformation of BCC metals and alloys. *Prog. Mater. Sci* 1992;36:29–61.
- [40] Meyers MA. Dynamic behavior of materials. *Exp. Mech* 2012;2:117–18.
- [41] Regazzoni G, Kocks U F, Follansbee P S. Dislocation kinetics at high strain rates. *Acta metall* 1987;35:2865–75.
- [42] Yao S, Pei X, Liu Z, Yu J, Yu Y, Wu Q. Numerical investigation of the temperature dependence of dynamic yield stress of typical BCC metals under shock loading with a dislocation-based constitutive model. *Mech. Mater* 2020;140:103211.
- [43] Qi L, Chrzan DC. Tuning ideal tensile strengths and intrinsic ductility of bcc refractory alloys. *Phys. Rev. Lett* 2014;112:115503.
- [44] Praveen S, Kim HS. Alloys High-Entropy. Potential Candidates for High-Temperature Applications - An Overview. *Adv. Eng. Mater* 2018;20:1700645.
- [45] Juan C, et al. Simultaneously increasing the strength and ductility of a refractory high-entropy alloy via grain refining. *Mater. Lett* 2016;184:200–3.